

## Article

# Evolution on the Microstructure and Mechanical Properties of a New Multicomponent Near-Alpha Titanium Alloy after Rolling and Heat Treatments

Jingyu Han <sup>1</sup>, Zhilei Xiang <sup>1</sup>, Xiaozhao Ma <sup>2</sup>, Zongyi Zhou <sup>1</sup>, Jingcun Huang <sup>1</sup>, Jihao Li <sup>1</sup>, Andong Wang <sup>1</sup>, Gaoliang Shen <sup>1</sup> and Ziyong Chen <sup>1,\*</sup> 

<sup>1</sup> College of Materials Science and Engineering, Beijing University of Technology, Beijing 100124, China

<sup>2</sup> AVIC Manufacture Technology Institute (MTI), Beijing 100024, China

\* Correspondence: czy@bjut.edu.cn; Tel./Fax: +86-010-67392880

**Abstract:** Near-alpha titanium alloys are widely used in aeroengine blades due to their excellent specific strength and mechanical properties. The mechanical properties of near- $\alpha$  titanium alloys are closely related to the evolution of the microstructure and precipitates. In this paper, the microstructure and mechanical properties of a new type of multi-component near- $\alpha$  titanium alloy sheet after rolling, 700 °C aging, and 800 °C aging were studied. The results show that the strength of the alloy after aging at 700 °C increases from 1156 MPa to 1304 MPa, respectively, but decreases to 1246 MPa with the aging temperature increasing. The ductility of the alloy aged at 700 °C is lower than that of the rolled state, but the ductility increases slightly with the aging temperature increasing. The effect of aging heat treatment on the microstructure and precipitation behavior of alloy plates has been studied and compared with alloys before aging. After heat treatment, the content of primary  $\alpha$  decreases from 25% to 5%, respectively. Two kinds of silicide precipitate at different positions, with the large-size spherical silicide being (Ti, Zr, Nb)<sub>5</sub>Si<sub>3</sub>, and the small-size fusiform silicide being (Ti, Zr, Nb)<sub>6</sub>Si<sub>3</sub>, respectively. Ti<sub>3</sub>Al was precipitated in the primary  $\alpha$  phase, during the aging process. The silicides exhibit the strengthening effect on the alloy, but the effect weakens when the silicides grow up. The loss in ductility is mainly attributed to the precipitation of the  $\alpha_2$  phase after aging treatment. However, ductility is improved after applying higher aging temperatures as the size of the  $\alpha_2$  phase becomes smaller, and the distribution of them tends to become dispersed.

**Keywords:** near- $\alpha$  high-temperature titanium alloy; microstructure; heat treatment; silicides;  $\alpha_2$  phase



**Citation:** Han, J.; Xiang, Z.; Ma, X.; Zhou, Z.; Huang, J.; Li, J.; Wang, A.; Shen, G.; Chen, Z. Evolution on the Microstructure and Mechanical Properties of a New Multicomponent Near-Alpha Titanium Alloy after Rolling and Heat Treatments. *Metals* **2023**, *13*, 1231. <https://doi.org/10.3390/met13071231>

Academic Editors: Francesca Borgioli and Tullio Monetta

Received: 22 February 2023

Revised: 9 June 2023

Accepted: 20 June 2023

Published: 4 July 2023



**Copyright:** © 2023 by the authors. Licensee MDPI, Basel, Switzerland. This article is an open access article distributed under the terms and conditions of the Creative Commons Attribution (CC BY) license (<https://creativecommons.org/licenses/by/4.0/>).

## 1. Introduction

Due to the excellent high-temperature performance of the near- $\alpha$  titanium alloy, it has been successfully applied in the aerospace field. Near- $\alpha$  titanium has been successfully applied in the aerospace field due to its excellent extreme-temperature performance [1]. Under the condition of solid solution aging (STA), the hardening precipitated phase, including silicide and the Ti<sub>3</sub>Al phase has a certain strengthening effect on the alloy [2,3]. Numerous reports have shown that the volume fraction, grain size, morphology, and distribution of the precipitation phase exhibit great effects on the mechanical properties of titanium alloys [4,5].

Near- $\alpha$  titanium alloys widely used at present can be classified as the Ti-Al-Sn-Zr-Mo-Si series [6]. These alloys are characterized by the addition of silicon to improve the tensile and creep properties at high temperatures [7]. Some typical near- $\alpha$  titanium alloys, such as the Ti6242S (Ti-6Al-2Sn-4Zr-2Mo-0.08Si, wt.%) alloy, the TIMETAL 834 (Ti-6Al-4Sn-3.5Zr-0.5Mo-0.7Nb-0.3Si, wt.%) alloy, the Ti60 (Ti-5.8Al-4.8Sn-2Zr-1Mo-0.85Nd-0.35Si, wt.%) alloy, and the Ti65 (Ti-5.8Al-3.8Sn-3.5Zr-0.5Mo-0.4Si-0.3Nb-2.0Ta-1W-0.05C, wt.%) alloy contain appropriate amounts of silicon. Silicon can significantly improve the strength and creep properties of near- $\alpha$  titanium alloys [8]. Hence, a moderate amount of Si is generally added

in high-temperature titanium alloys. Si typically exists in the form of solid solution and silicide in high-temperature titanium alloys, which can be converted into each other under certain conditions. Two kinds of silicide, including  $Ti_5Si_3$  (S1 type) and  $Ti_6Si_3$  (S2 type) exist in the form of high-temperature titanium [9,10]. Silicide precipitates are mainly involved in the process of heat treatment, heat exposure, and hot working along with the evolution of microstructure [11]. Aluminum mainly plays a role in stabilizing the  $\alpha$  phase and providing solid solution strength in the near- $\alpha$  titanium alloy. Around 7 wt.% (11.8 at. %) of the Al component was generated by phase separation, which meant at temperatures of 500–700 °C, crystallographic ordering of Al can occur, and lead to precipitation of the  $Ti_3Al$  ( $\alpha_2$ ) phase [12]. Commonly, the strength and creep resistance of the titanium alloy can be improved by the  $\alpha_2$  precipitate-strengthening mechanism. However, as with any other intermetallic phase, the  $\alpha_2$  phase is brittle, and leads to a reduction in its ductility. In order to limit the proportion of  $\alpha_2$  precipitated from the  $DO_{19}$  structure, the Al content was controlled at about 6% [13].

In addition to controlling the composition, the proportion of the primary and secondary lamellar  $\alpha$  phase in the matrix, and the size and distribution of micro and nano precipitates, including silicide and the  $\alpha_2$  phase can also be changed by adjusting the aging temperature and time. Thus, the properties of the alloy can be improved as a result. For example, A. Radecka [14] found that the morphology of ordered  $Ti_3Al$  particles precipitated at 550–700 °C is different. The dislocation must pass through the coherent interface between the  $Ti_3Al$  particle and the matrix, which results in the effect of strengthening the matrix. After the application of the solution and aging treatment of  $Ti_{65}$ ,  $(Ti, Zr)_6(Si, Sn)_3$  silicide precipitates along  $\alpha/\beta$  interface, and  $Ti_3Al$  particles are dispersed in the  $\alpha$  matrix with a particle size of about 1.4 nm. Finally, the ultimate tensile strength of the  $Ti_{65}$  alloy can reach to 1253 MPa [15]. In this study, the microstructure and mechanical properties (strength and plasticity) of a new multicomponent near-alpha titanium alloy were affected by hot working and solution aging treatment. Through the analysis of the microstructure characteristics, tensile properties, fracture morphology, and the interaction between the dislocations and precipitates before and after the hot working of the alloy, the mechanism of strength and plasticity changes of the alloy was thoroughly elucidated. This work provides guidance for developing thermal exposure and ensuring thermal stability of near- $\alpha$  titanium alloys.

## 2. Materials and Methods

In this study, a new multi-component near-alpha titanium alloy  $Ti-6.5Al-2.5Sn-9Zr-0.5Mo-0.25Si-1Nb-1W-0.1Re$  with 5 kg was acquired using the induction skull melting (ISM) [16] technique three times to ensure the homogeneity of alloy. The  $\beta$  transus temperature ( $T_\beta$ ) was determined as 1003 °C with metallographic analysis. The casting-riser of 5 kg ingot was cut with the wire-electrode cutting technique, and then the ingot was adopted to the blooming forge at 980 °C, which takes place at the  $\alpha + \beta$  phase region. After blooming forging, the ingot was preserved in a box-type resistance furnace at 980 °C for 40 min. Then, the secondary forging process was performed, with the reductions being 40%, 30%, and 30% on the directions perpendicular to three orthogonal planes, respectively. Next, these processes were repeated for a further two times. Reheating at 980 °C for 10 min was conducted after every two steps of forging processes. Air cooling was adopted after this secondary forging stage. The final dimensions of ingot was 185 mm  $\times$  46 mm  $\times$  30 mm. The rectangular specimens were hot-rolled with a total height reduction of 60% through 12 passes on the rolling direction (RD). The final dimension of the rolled plate in all direction was 425 mm  $\times$  50 mm  $\times$  12 mm, and the specimen was air-cooled after all passes.

The raw materials of the unaged and aged samples were all obtained from hot-rolled plates. The mill model was a YZ-2310 two-high mill. The roll diameter of the mill was 310 mm, the maximum bite amount of the roll was 30 mm, and the rolling speed was 15 RPM, respectively. Three kinds of samples were assessed in this experiment. Two rough samples were solution treated at 990 °C for 1 h and then cooled in the air. Subsequently, they

were aged at 700 °C and 800 °C for 4 h separately, followed by air cooling (AC). Another sample was left unaged. The geometric size of the tensile sample at room temperature is shown in Figure 1. The tensile specimens with the size of 20 × 30 mm (parallel to RD) and gauge length ( $L_0$ ) of 25 mm were assessed on a DDL50 universal testing machine along the TD direction with the strain rate of  $5 \times 10^{-4} \text{s}^{-1}$  at room temperature.

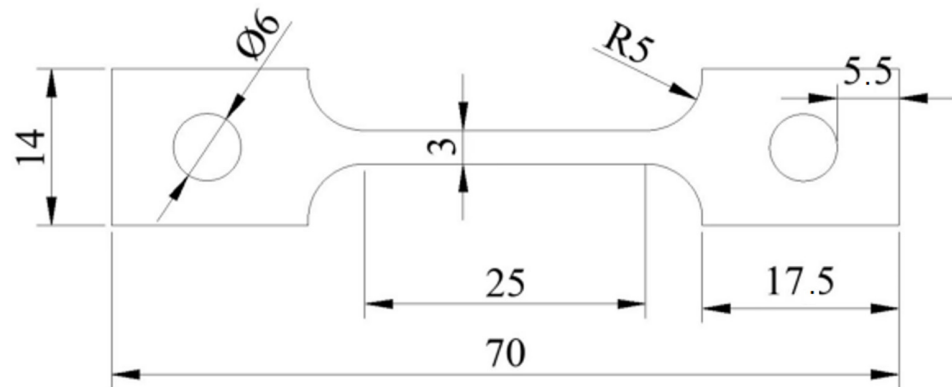


**Figure 1.** Geometrical dimensions of the tensile specimens at room temperature.

The microstructure characteristics and the precipitation behavior of the samples were assessed using scanning electron microscope (SEM), energy dispersive X-ray spectroscopy (EDS), and transmission electron microscopy (TEM). Specimens used for TEM tests were fabricated by the two-jet electro-chemical polishing processes using the electrolyte of 5% perchloric, 35% butanol, and 60% methanol at  $-20$  °C and 53 V, respectively. In this study, The content of the equiaxed  $\alpha_P$  in the alloy was calibrated using Image Pro plus version 6.0 software.

### 3. Results

#### 3.1. Microstructure Evolution during Aging Process

The SEM images of the as-casting microstructure are shown in Figure 2. The as-casting alloy exhibits a typical Widmanstätten structure, and the average size of the prior  $\beta$  grain is about 261  $\mu\text{m}$ . In Figure 2a, clear triangular grain boundaries which is marked by a yellow arrow can be seen at the prior  $\beta$  grain. In addition, in Figure 2b, large  $\alpha$  phase clusters are interlaced within the  $\beta$  grain. [17]. The SEM images of the alloy after the rolling and different heat treatment systems are shown in Figure 3, respectively. Large  $\beta$  grains and obvious  $\beta$  grain boundaries, as shown in Figure 1, have been broken down and disappeared. The rolling state of the alloy exhibits the typical characteristics of a duplex microstructure. Figure 3a shows that the equiaxed  $\alpha$ -phase was mainly concentrated in a linear form. Due to the dynamic recovery and recrystallization [18] during the rolling process, a number of fine  $\alpha$  lamellae were densely arranged in the equiaxed  $\alpha$  grain gap [19]. Therefore, the rolled microstructure of the alloy was mainly composed of the equiaxed  $\alpha$  phase, the secondary strip  $\alpha$ , and the residual  $\beta$  phase. The microstructure of the alloy sheet clearly changed after aging. As shown in Figure 3b, compared with the rolled alloy, the content of the equiaxed  $\alpha$  phase reduced from 25% to 5%, respectively, while the content of the  $\beta$  transition microstructure (lamellar  $\alpha$  phase and grain boundary phase) increased significantly. As shown in Figure 3b, after heat treatment, the content of equiaxed  $\alpha$  phase decreases from 25% to 5%, while the content of  $\beta$  transition structure (lamellar  $\alpha$  phase and grain boundary phase) significantly increases compared with the rolled alloy. After increasing the aging temperature, the content of equiaxed  $\alpha$  phase did not change much, as shown in Figure 3c. Combined with the TEM images in Figure 4, it can be seen that the secondary lamellar  $\alpha$  phase markedly grows. The lamellar width of the secondary lamellar  $\alpha$  phase also increases with the increase in the aging temperature. It is known that the size and content of the  $\alpha$  lamellae can affect the yield strength by changing the distances between the boundaries for dislocation motion. When comparing the TEM images of the

unaged and aged alloys, it can be found that the entanglement and interlacing of the  $\alpha$  layer and the dislocation after rolling in the unaged alloys is not so clear. After aging at 700 °C in Figure 4b, the  $\alpha$  lamellar prevent the dislocation movement, and dislocation itself accumulates [20] at the boundary of the adjacent  $\alpha$  lamellar crystals. With the increase in the aging temperature, the interlacing effect observed between the dislocation and lamellar is further enhanced in combination with Figure 4c,f, A high-density dislocation structure similar to the dislocation wall is then formed as a result [21].

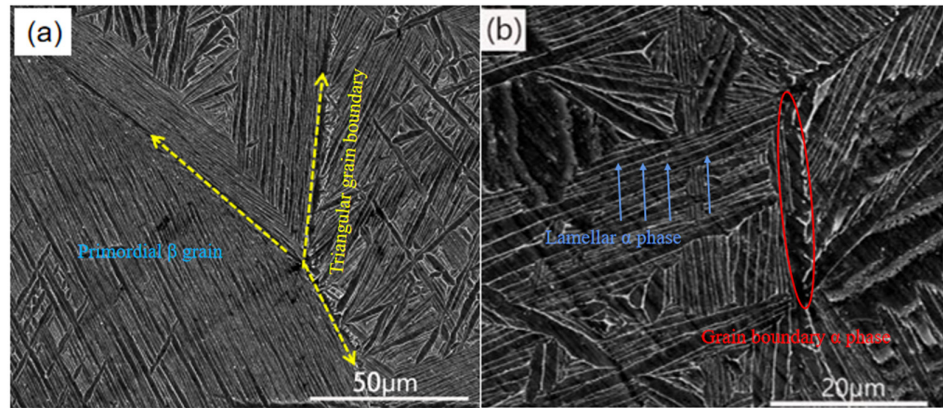


Figure 2. SEM morphology of the as-cast alloy. (a) Grain boundary, and (b)  $\alpha$  lamellar cluster.

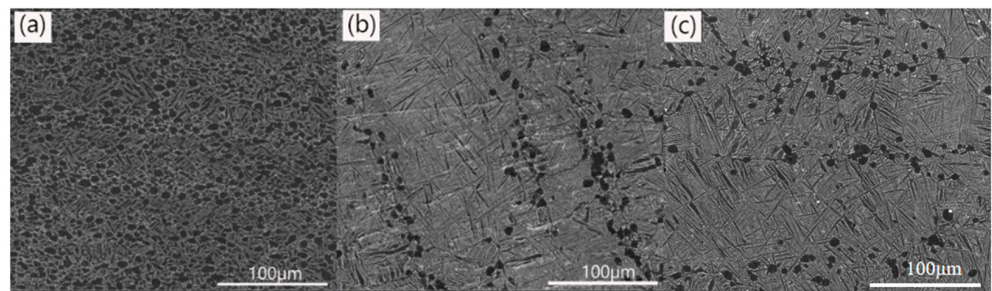


Figure 3. SEM image of the alloy sheet: (a) rolled, (b) aged at 700 °C for 4 h, (c) aged at 800 °C for 4 h.

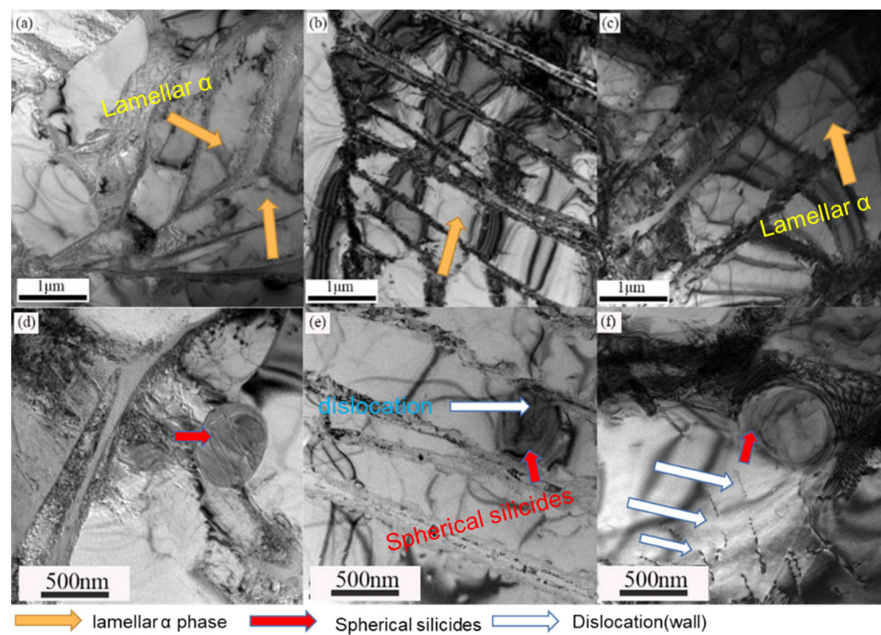


Figure 4. TEM images of the matrix and silicide in the alloy sheet: (a,d) rolled; (b,e) aged at 700 °C for 4 h; (c,f) aged at 800 °C for 4 h.

### 3.2. Evolution Process of Nano-Precipitation

From Figure 4d–f, it can be seen that large-scale phase particles are generated during the rolling and aging processes. Combined with the EDS diagram in Figure 5, it can be clearly seen that silicon is enriched in the particles, and thus it can be preliminarily judged as silicide. After the selected area electron diffraction (SAED) spot calibration, its structure can be determined as the  $(\text{Ti, Zr})_5\text{Si}_3$  phase with a densely packed hexagonal structure, and the size of this phase is 0.3–1.2  $\mu\text{m}$  [22,23]. Most of these silicides are distributed between the  $\alpha$  lamellar phase boundaries, while a minor part is distributed at the boundary edge of the equiaxial  $\alpha$  phase. The SAED pattern of the spherical silicide is shown in Figure 6b. After aging at different temperatures, the morphology of the spherical silicide has no obvious change, but the size increases from 700 nm to 800 nm, respectively, with the increase of temperature. Figure 7 shows another silicide in the alloy, which is fusiform in shape, with a length-to-diameter ratio of 2.8 and a size of 100–200 nm, respectively. The crystal structure was subsequently identified as the  $(\text{Ti, Zr})_6\text{Si}_3$  [24] phase after SAED diffraction spot calibration.

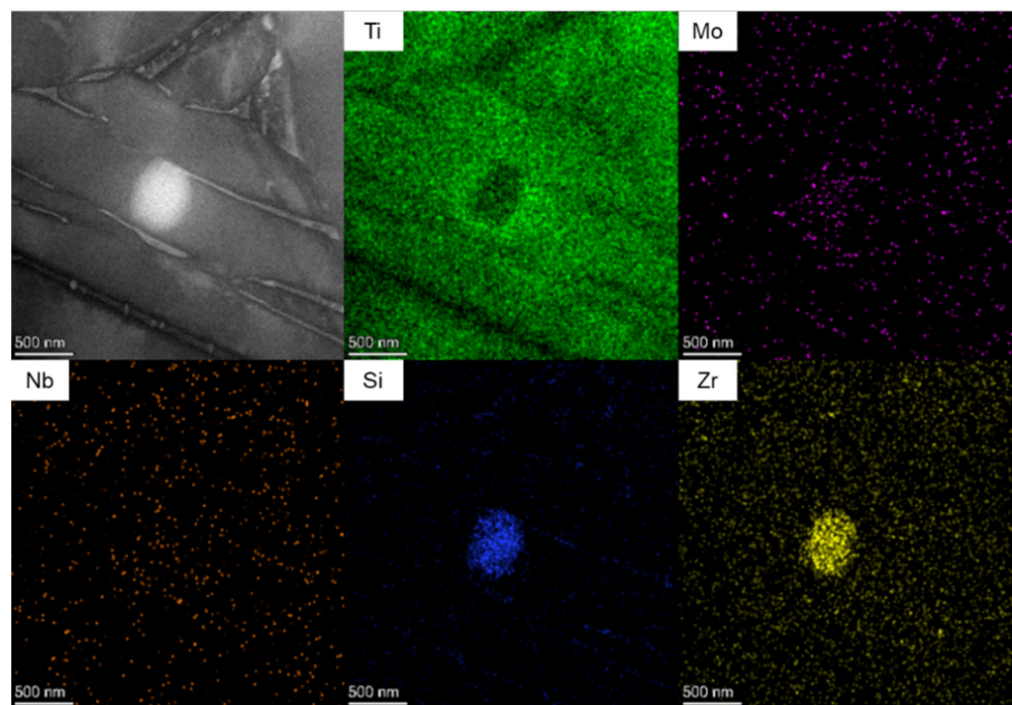


Figure 5. EDS distribution of elements in the silicide.

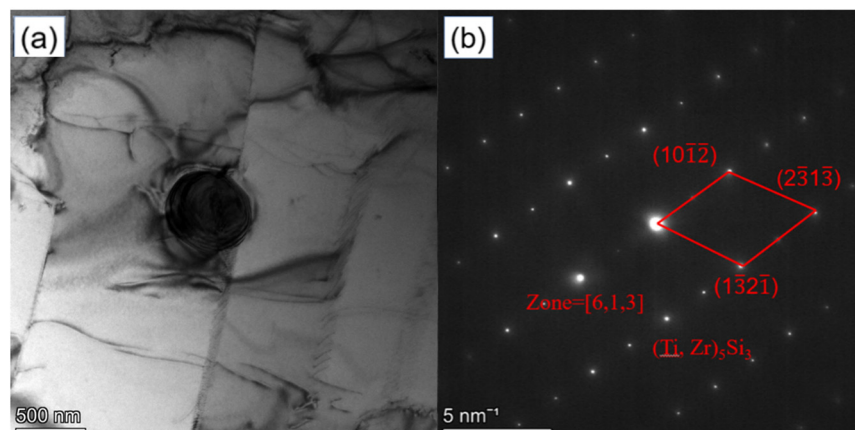
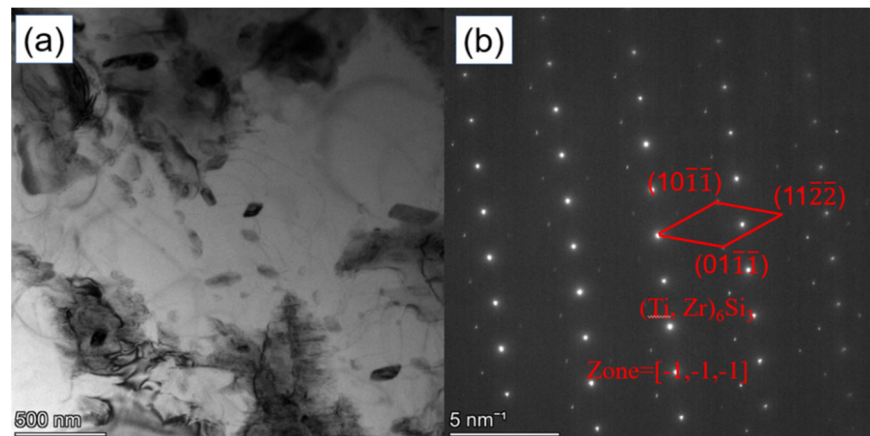
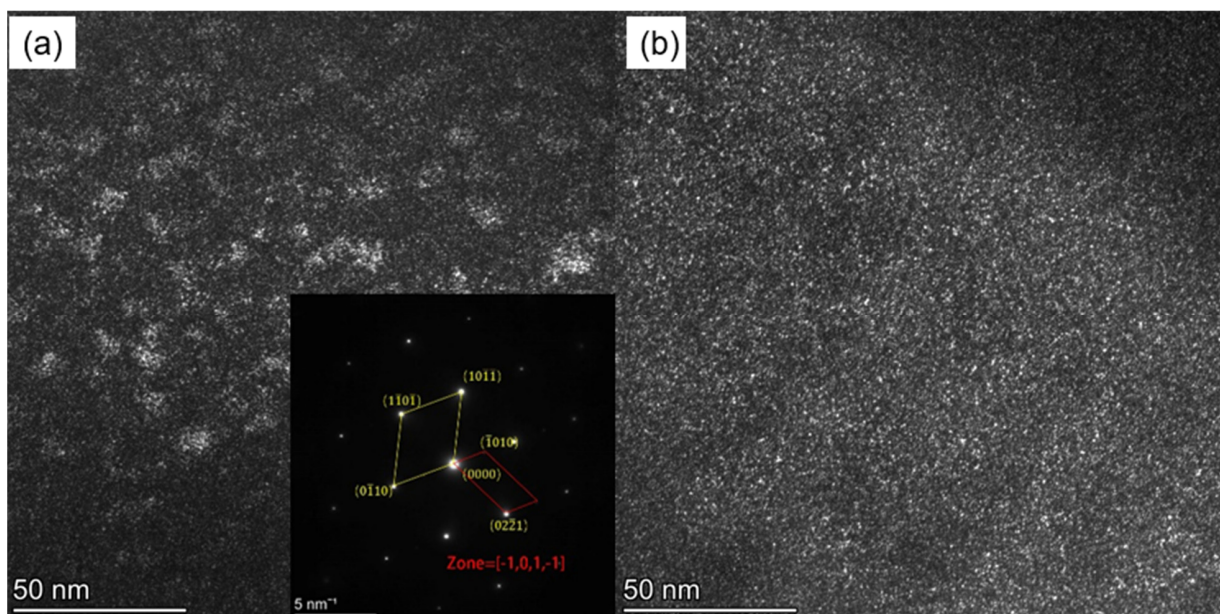


Figure 6. TEM images of silicide: (a) spheroidal incoherent silicide; (b) the SEAD pattern of the silicide.



**Figure 7.** TEM images of silicide: (a) fusiform silicide; (b) the SEAD pattern of the silicide.

Additionally, the superlattice spots imply that the  $\text{Ti}_3\text{Al}$ -ordered phase encompassing a HCP structure precipitates in the HCP titanium matrix [25,26]. By comparing the characteristics of  $\text{Ti}_3\text{Al}(\alpha_2)$  phase aged at different temperatures, as shown in Figure 8, in the alloy aged at  $700^\circ\text{C}$ , the size of the second phase  $\text{Ti}_3\text{Al}$  is too small to be counted, and the  $\text{Ti}_3\text{Al}$  particles show a state of aggregation. When aging temperature rose to  $800^\circ\text{C}$ , the size of the  $\text{Ti}_3\text{Al}(\alpha_2)$  phase particles negligibly changed, and the originally aggregated particles became more dispersed. Therefore, with the increase in the aging temperature, the size of the  $\text{Ti}_3\text{Al}(\alpha_2)$  phase increases and the particles become relatively dispersed as a result.



**Figure 8.** TEM images of the  $\alpha_2$  phase: (a) aged at  $700^\circ\text{C}$  for 4 h, the SEAD pattern of matrix is inserted in (a); and (b) aged at  $800^\circ\text{C}$  for 4 h.

### 3.3. Mechanical Property Analysis

Figure 9 displays the mechanical properties of Cast-A, R-A, 700-A, and 800-A at RT, respectively, along with a set of experimental data, including the corresponding values of the tensile property parameters, ultimate tensile strength (UTS), yield strength (YS), and elongation (EL) are summarized in Table 1. The tensile strength (UTS) of the alloy was increased from 1156 MPa to 1304 Mpa, respectively, when comparing the curves of the unaged and  $700^\circ\text{C}/4\text{ h}$  aging. When the aging temperature increased, the tensile strength (UTS) of the alloy sheet decreased to about 50 MPa. On the other hand, when examining

the alloy from R-A to 700-A, elongation decreased from 12.0% to 9.1%, respectively. With further increases in the temperature, only little changes in elongation were observed.

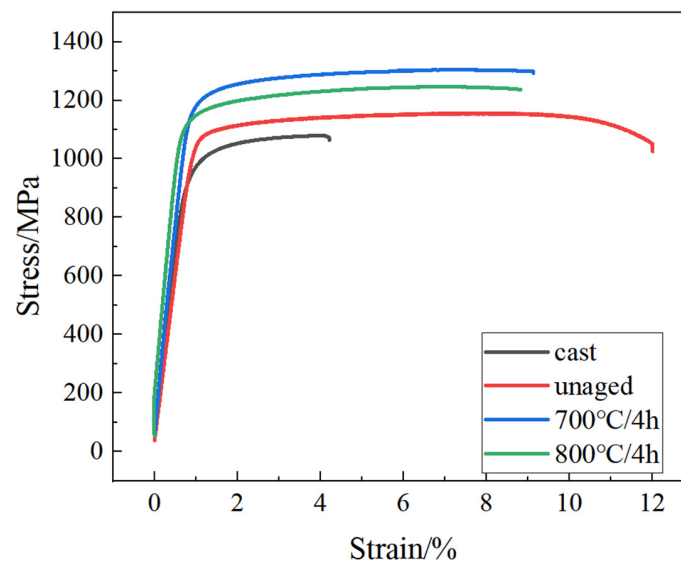


**Figure 9.** Tensile stress–strain curves of the alloy sheet (1\* samples in Table 1) performed at room temperature.

**Table 1.** Tensile properties of alloy sheets at room temperature. In order to make a clear mark for the sample, the alloy in each state is divided into 1\* and 2\* two samples.

Alloys		YS (MPa)	UTS (MPa)	EL (%)
Cast-A	1 *	951	1088	7.7
Cast-A	2 *	957	1079	4.2
Average		954	1084	6.0
R-A	1 *	1069	1156	12.0
R-A	2 *	1056	1148	10.5
Average		1063	1152	11.3
700-A	1 *	1178	1304	9.1
700-A	2 *	1222	1275	8.3
Average		1200	1290	8.7
800-A	1 *	1118	1246	8.8
800-A	2 *	1105	1230	9.0
Average		1112	1238	8.9

### 3.4. Fracture Morphology

The differences in the tensile strength and elongation are also accompanied with the differences in fracture morphology. As shown in Figure 10, the tensile fracture morphology of the as-cast alloy on the whole is a brittle fracture. In Figure 10a, pits on the surface of the fracture were observed, which were mainly caused by the common defects of the as-cast structure. In addition, obvious tearing edges were also present on the fracture surface. Combined with the elongation, it can be thereby preliminarily judged as a brittle fracture, and due to the coarse grains and obvious grain boundaries in the alloy, it is mainly an intergranular fracture. Figure 10b shows that the uneven stepped edge is the typical characteristic of a brittle fracture. Figure 11 shows the SEM images of tensile specimens at room temperature under rolled and aged conditions. According to the overall morphology of the fracture in Figure 11a, the surface of the fracture was smoother than that of the as-cast state, and there was no obvious tearing edge due to the absence of coarse original grains in the microstructure after hot processing. Combined with the table of mechanical properties listed in Table 1, Figure 11b shows that the fracture mode is a ductile fracture with a large number of dimples in the fracture. The globular incoherent silicides  $(\text{Ti,Zr})_6\text{Si}_3$

was considered as a brittle precipitate [26,27], which generally contributes to the expansion of the quasi-cleavage area. The globular incoherent  $(\text{Ti, Zr})_6\text{Si}_3$  silicide plays the role of the origin of micro cavities, from which these cavities grow and coalesce to form dimples [28]. During the aging process of  $700\text{ }^\circ\text{C}/4\text{ h}$ , as shown in Figure 11e, the number of dimples decreased significantly, while the number of silicides also decreased. However, the biggest change in the aging state compared with the rolling state was that the content of the lamellar  $\alpha$  structure increased. Therefore, these clear lamellar clusters can be observed in the tensile fracture of the  $700\text{ }^\circ\text{C}/4\text{ h}$  aging state. These clusters increase strength and provide a good degree of ductility. Therefore, after  $700\text{ }^\circ\text{C}/4\text{ h}$  aging, the alloy still maintains a high elongation of 9.13%. After  $800\text{ }^\circ\text{C}/4\text{ h}$  aging, the size of dimples and the number of quasi cleavage planes increased, while the number of dimples decreased.

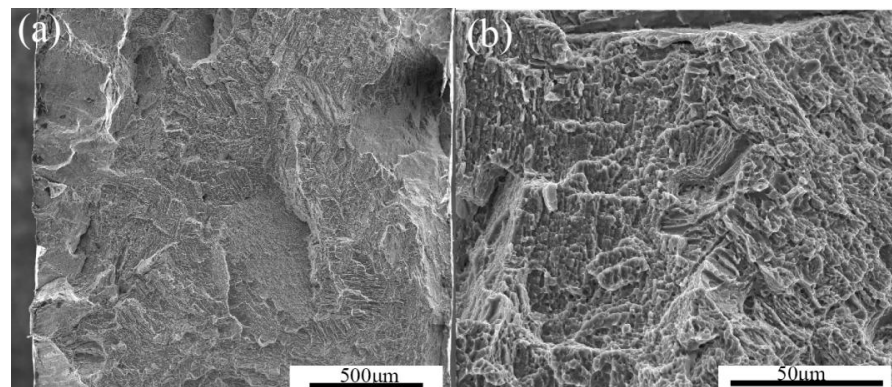


**Figure 10.** Tensile fracture morphology of the casting state.

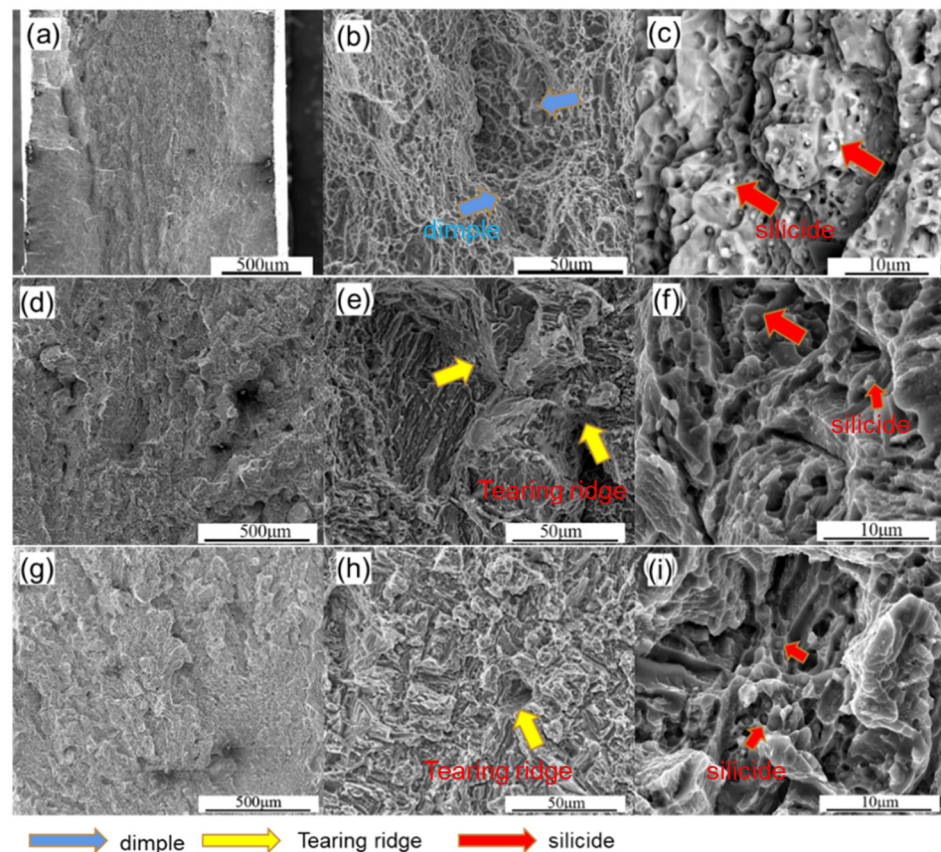


**Figure 11.** Tensile fracture morphology: (a–c) unaged; (d–f) aged at  $700\text{ }^\circ\text{C}$  for 4 h; and (g–i) aged at  $800\text{ }^\circ\text{C}$  for 4 h.

## 4. Discussion

### 4.1. Effect of Precipitation on the Overall Strength of the Alloy

The interaction mechanism between these precipitates and dislocations was analyzed and explained through characterizing the samples using SEM, TEM, and the tensile test. Two kinds of silicide have been defined in the previous article [28,29]. The structure of these two silicides is a hexagonal structure. The chemical formula of large-size silicides is  $(\text{Ti,Zr})_5\text{Si}_3$  ( $a = 0.7429$ ,  $c = 0.5139$ ), and the size ranges from 0.3~1.2  $\mu\text{m}$ , respectively. The chemical formula of the small-size silicide is  $(\text{Ti,Zr})_6\text{Si}_3$  ( $a = 0.7010$ ,  $c = 0.3680$ ), and the size ranges from 100 nm to 200 nm, respectively. The precipitation state of the silicide will have a certain effect on the strengthening of the alloy. The strengthening mechanism of the alloy needs to be analyzed in the three stages of alloy rolling, 700 °C aging, and 800 °C aging, respectively. The first is the rolling stage, Due to the rolling temperature of 980 °C, which is close to the  $\beta$  transition point, the equiaxed  $\alpha$  content can effectively controlled at about 25% after forging near  $\beta$  [30], meaning that the alloy can obtain a better match of strength, plasticity, and toughness than the casting state. According to Table 1, the reason for the obvious improvement in the strength and plasticity of the alloy after rolling is the change of the Weissmann microstructure to a bimodal microstructure. Figure 12 shows that large-size silicides were found between  $\alpha_p$  and  $\alpha_s$ . Additionally, no obvious nailing effects on the silicide and dislocation entanglement were found in the microstructure of the rolled alloy.

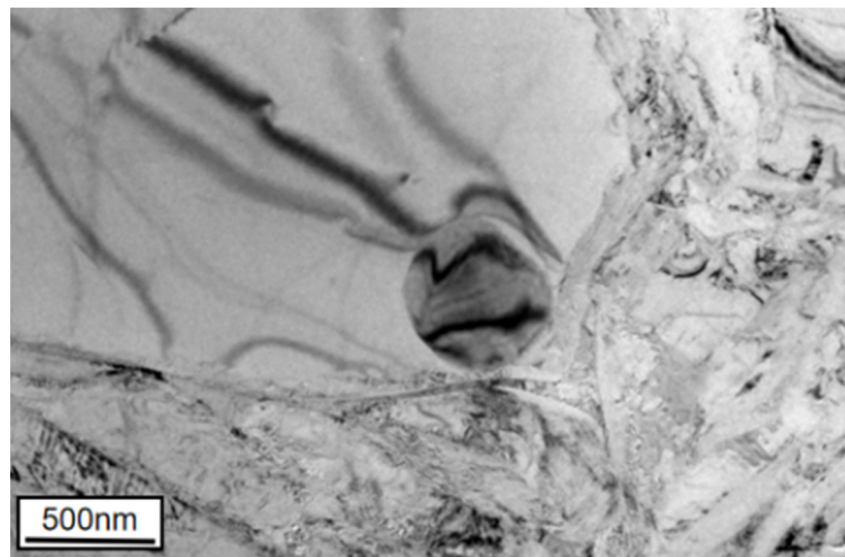


**Figure 12.** Silicide morphology of the unaged alloy.

At 700 °C for 4 h, the increases in strength of the aged sheet can be attributed to interface strengthening [31], interfacial silicide, and  $\text{Ti}_3\text{Al}$  precipitation strengthening. As shown in Figure 13a, a few dislocations were distributed inside and in between the secondary lamellar  $\alpha$ , which was combined with the dislocation strengthening formula:

$$\tau = \tau_0 + \alpha Gb\rho^{1/2}$$

The parameters in the formula are expressed separately ( $\rho$ : dislocation density;  $G$ : shear modulus;  $b$ : Burgers vector; and  $\alpha$ : coefficient) [32]. It can be seen that  $\tau$  increases as  $\rho$  increases. Figure 13b shows that the dislocation cut through the silicide particles, which thereby hinders the subsequent slip and produces a strengthening effect as a result. Figure 13c shows that a small-size silicide  $(\text{Ti,Zr})_6\text{Si}_3$  was precipitated between the  $\alpha_s$ , and there is an obvious dislocation entanglement around it. Some dislocations were found to cut through the silicide particle. Therefore, when the dislocation encounters particles and slips are obstructed, the external shear stress must therefore be increased to

overcome the increase in the dislocation line tension caused by dislocation bending. Elastic interaction occurs between the coherent stress field of the precipitated particles and the stress field of dislocation, and certain strengthening effects occur when dislocation passes through the coherent strain zone. Another nano precipitate,  $\text{Ti}_3\text{Al}$ , is precipitated after solution aging treatment. The selected area diffraction pattern indicates that the ordered  $\alpha_2$  phase precipitated from the  $\alpha$  matrix. The dark-field micrograph of  $\text{Ti}_3\text{Al}$  and its selected area diffraction pattern are shown in Figure 8. where the particle size is small, certain aggregation occurs, and the size of the  $\text{Ti}_3\text{Al}$  particle cluster formed by the aggregation is about 2 nm.  $\text{Ti}_3\text{Al}$  particles can improve the strength of the matrix through the strain field generated by the dislocation interaction [33].

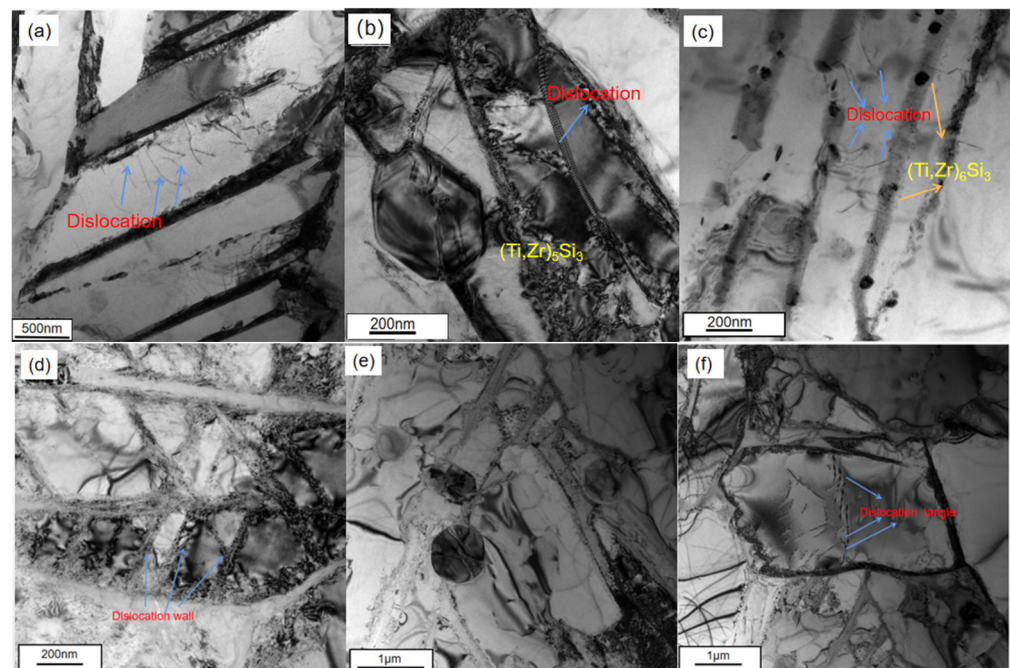


**Figure 13.** Entanglement effect of dislocations in alloys (a–c) 700 °C/4 h; (d–f) 800 °C/4 h; (a) lamellar alpha; (b)  $(\text{Ti,Zr})_5\text{Si}_3$ ; (c)  $(\text{Ti,Zr})_6\text{Si}_3$ ; (d) lamellar alpha; (e)  $(\text{Ti,Zr})_5\text{Si}_3$  (f) dislocation primary alpha.

As the aging temperature rises to 800 °C, the content and size of the equiaxed  $\alpha$  phase negligibly changed. Compared with the alloy aged at 700 °C/4 h, the contribution of the equiaxed  $\alpha$  phase was deemed to be little. As shown in Figure 13d, a high-density dislocation wall was formed between the lamellar phases, resulting in the production of a clear dislocation strengthening effect. Figure 13e shows that no significant changes were observed in the shape or size of the silicide. From Figure 13f, high-density dislocations accumulated in the  $\alpha_p$ , which can markedly strengthen the matrix as a result. Combined with Table 1, the most obvious change observed after the aging temperature rose was the decrease in strength, especially in the yield strength, which decreased by 80 MPa on average. This was mainly because the yield strength, i.e., the dislocation overcomes the stress required by the surrounding Coriolis air mass. As the temperature increases, the nailing effect of the Coriolis air mass on the dislocation is weakened, and the force required for dislocation slip is subsequently reduced, which is represented by the reduction in the yield strength on a macro level. In addition, the  $\alpha_2$  phase was also observed within the matrix of the alloy aged at 800 °C/4 h, as shown in Figure 8. The size of the nanoscale precipitated phase did not change much, but the distribution state became more dispersed. As a result, the motion of dislocation was hindered by the dispersed precipitated particles, signifying that the strength of the alloy will be significantly improved. Previous studies have stated that the dispersion of the  $\alpha_2$  phase with a fine size distribution contributes to the strengthening of the alloy [34].

#### 4.2. The Precipitate Effects on the Overall Ductility in the Alloy

The ductility of the whole alloy was closely related to the change in the alloy matrix and the second phase. The change in the ductility of the alloy was also divided into three stages. The first was the change from the as-cast stage to the rolled stage, resulting in significant improvements to the ductility of the alloy. With the observation of changes in the microstructure of the alloy from the Widmanstätten structure to a binary microstructure, this thereby marks the clear improvements in ductility. After aging at 700 °C for 4 h, the elongation in the alloy sheet was found to be lower than that in the rolled state. Furthermore, Figure 10b,c, show that the content of the equiaxed  $\alpha$  phase decreased from 25% to 5%, respectively, and that the content of the  $\beta$  transition microstructure clearly increased. Therefore, the elongation of the alloy decreased as a result. The  $\alpha_2$  ( $\text{Ti}_3\text{Al}$ ) phase was formed in the alloy. Due to the anisotropy of the  $\alpha_2$  phase, it is easy to localize slip, resulting in the poor ductility of the alloy. When aging temperature was increased to 800 °C, as shown in Figure 3, the morphology and content of the equiaxed  $\alpha$  phase negligibly changed. In addition, the morphology and size of the globular incoherent silicide did not change much compared with that observed in 700 °C, indicating that it has little influence on the ductility of the alloy. However, as shown in Figure 8, the distribution of the  $\alpha_2$  phase in the matrix became more diffuse. Combined with the previous researches, the  $\alpha_2$  phase, with a small size and uniform precipitation distribution in the matrix not only contributes to the strengthening of the alloy [35], but also does not reduce the ductility of the alloy, which is consistent with the experimental results.

#### 5. Conclusions

In this study, the strength of the alloy was greatly improved by the aging treatment. Through the characterization and analysis of the microstructure, phase precipitation behavior, dislocation slip characteristics, and fracture morphology, the strengthening and toughening mechanisms of the alloy were revealed. The following conclusions can be drawn:

- (1) Compared with the as-cast alloy, the microstructure of the matrix changes from the Widmanstätten structure to a duplex structure after rolling. The primary  $\beta$  grains are broken, the content of equiaxed  $\alpha$  phase is 25%, and the secondary lamellar  $\alpha$  phase is formed. After solution at 990 °C and aging at 700 °C, the content of equiaxed  $\alpha$  phase decreases to about 5%;
- (2) The strength of the new multicomponent near-alpha titanium alloy is improved by aging at 700 °C for 4 h. The UTS increased by 12.0% (from 1152 MPa to 1290 MPa, respectively), and the elongation decreased by 2.7% (from 11.3% to 8.3%, respectively). With increasing the aging temperature to 800 °C, the elongation slowly increased (from 8.3% to 8.9%, respectively);
- (3) The strength of the alloy is enhanced by the dispersion strengthening of the dual-scale silicide precipitates, but this effect weakens with the growing up of the grain size. The  $\text{Ti}_3\text{Al}$  ( $\alpha_2$ ) phase precipitates after aging exhibit adverse effects on the ductility. However, the dispersion of the  $\text{Ti}_3\text{Al}$  ( $\alpha_2$ ) phase particles is conducive to the recovery of the ductility at 800 °C aging. Although this paper ensures the plasticity and improves the strength of the alloy to a certain extent, the thermal stability after long-term use must also be the focus of research if it is to be applied to aero-engine components, and needs to be further explored in the future.

**Author Contributions:** J.H. (Jingyu Han): Conceptualization, Writing—original draft. Z.X.: Methodology. X.M.: Data curation. Z.Z.: Software. J.H. (Jingcun Huang): Investigation. J.L.: Resources. A.W.: Software. G.S.: Resources. Z.C.: Supervision. All authors have read and agreed to the published version of the manuscript.

**Funding:** This research was funded by National Natural Science Foundation of China (No. 51870191), and the Industrial Strengthen Foundation Project of Ministry of Industry and Information Technology, PRC (TC150B5C0-02).

**Data Availability Statement:** The raw/processed data required to reproduce these findings cannot be shared at this time as the data also forms part of an ongoing study.

**Acknowledgments:** The authors would like to gratefully acknowledge the supports of the National Natural Science Foundation of China (No. 51870191), and the Industrial Strengthen Foundation Project of Ministry of Industry and Information Technology, PRC (TC150B5C0-02).

**Conflicts of Interest:** The authors declare that they have no known competing financial interests or personal relationships that could have appeared to influence the work reported in this paper.

## References

1. Peters, M.; Hemptenmacher, J.; Kumpfert, J.; Leyens, C. *Structure and Properties of Titanium and Titanium Alloys*; Wiley-VCH Verlag GmbH & Co. KGaA: Weinheim, Germany, 2003.
2. Srinadh, K.V.S.; Singh, V. Oxidation behaviour of the near  $\alpha$ -titanium alloy IMI 834. *Bull. Mater. Sci.* **2004**, *27*, 347–354. [[CrossRef](#)]
3. Evans, R.W.; Hull, R.J.; Wilshire, B. The effects of alpha-case formation on the creep fracture properties of the high-temperature titanium alloy IMI834. *J. Mater. Process. Technol.* **1996**, *56*, 492–501. [[CrossRef](#)]
4. Cremasco, A.; Andrade, P.N.; Contieri, R.J.; Lopes, E.S.N.; Afonso, C.R.M. Correlations between aging heat treatment,  $\omega$  phase precipitation and mechanical properties of a cast Ti–Nb alloy. *Mater. Des.* **2011**, *32*, 2387–2390. [[CrossRef](#)]
5. Wang, L.; Lu, W.; Qin, J.; Zhang, F.; Zhang, D. Effect of precipitation phase on microstructure and superelasticity of cold-rolled beta titanium alloy during heat treatment. *Mater. Des.* **2009**, *30*, 3873–3878. [[CrossRef](#)]
6. Zhang, S.; Wang, B.; Liu, Z.; Gao, Y.; Yang, R. Effect of carbon on microstructures and mechanical properties of Ti-60 high-temperature titanium alloy. *Chin. J. Mater. Res.* **2007**, *21*, 433–438.
7. Peng, W.W.; Zeng, W.D.; Wang, Q.J.; Yu, H. Comparative study on constitutive relationship of as-cast Ti60 titanium alloy during hot deformation based on Arrhenius-type and artificial neural network models. *Mater. Des.* **2013**, *51*, 95–104. [[CrossRef](#)]
8. Wang, Q.J.; Liu, J.R.; Yang, R. High Temperature Titanium Alloys Status and Perspective. *J. Aeronaut. Mater.* **2014**, *34*, 1–26.
9. Jiao, Y.; Huang, L.; Wei, S.L.; Peng, H.; An, Q.; Jiang, S.; Geng, L. Constructing two-scale network microstructure with nano-Ti5Si3 for superhigh creep resistance. *J. Mater. Sci. Technol.* **2019**, *35*, 11. [[CrossRef](#)]
10. Narayana, P.L.; Kim, S.W.; Hong, J.K.; Reddy, N.S. Tensile properties of a newly developed high-temperature titanium alloy at room temperature and 650 °C. *Mater. Ence Eng. A* **2018**, *718*, 287–291. [[CrossRef](#)]
11. Su, Y.; Kong, F.; You, F.; Wang, X.; Chen, Y. The high-temperature deformation behavior of a novel near- $\alpha$  titanium alloy and hot-forging based on the processing map. *Vacuum* **2020**, *173*, 109135. [[CrossRef](#)]
12. Huang, Y.C.; Suzuki, S.; Kaneko, H.; Sato, T. Thermodynamics of the M s points in titanium alloys. *Sci. Technol. Appl. Titan.* **1970**, *20*, 691–693.
13. Palm, M.; Schuster, J.C. Reassessment of the Ti–Al Phase Diagram. In Proceedings of the 3rd international Workshop on g-TiAl Technologies, Bamberg, Germany, 29–31 May 2006.
14. Radecka, A.; Bagot, P.A.J.; Martin, T.L.; Coakley, J.; Vorontsov, V.A.; Moody, M.P.; Ishii, H.; Rugg, D.; Dye, D. The formation of ordered clusters in Ti7Al and Ti6Al4V. *Acta Mater.* **2016**, *112*, 141–149. [[CrossRef](#)]
15. Yue, K.; Liu, J.; Zhu, S.; Wang, L.; Wang, Q.; Yang, R. Origins of different tensile behaviors induced by cooling rate in a near alpha titanium alloy Ti65. *Materialia* **2018**, *1*, 128–138. [[CrossRef](#)]
16. Rack, H.J.; Qazi, J.I. Titanium alloys for biomedical applications. *Mater. Sci. Eng. C* **2006**, *26*, 1269–1277. [[CrossRef](#)]
17. Mathabathe, M.N. Cold-pressing and vacuum arc melting of  $\gamma$ -TiAl based alloys. *Adv. Powder Technol.* **2019**, *30*, 2925–2939. [[CrossRef](#)]
18. Ma, X.; Xiang, Z.; Tan, C. Influences of boron contents on microstructures and mechanical properties of as-casted near  $\alpha$  titanium alloy. *J. Mater. Sci. Technol.* **2021**, *77*, 1–18. [[CrossRef](#)]
19. Sun, Y.; Zhang, C.; Feng, H. Dynamic recrystallization mechanism and improved mechanical properties of a near  $\alpha$  high temperature titanium alloy processed by severe plastic deformation. *Mater. Charact.* **2020**, *163*, 110281. [[CrossRef](#)]
20. Jaffee, R.I. *The Science, Technology and Application of Titanium*; Pergamon Press: Oxford, UK, 1970.
21. Ma, T.F.; Zhou, X.; Li, L.; Zhang, L.C.; Zhang, Y.S.; Zhang, P.X. High temperature deformation and microstructural evolution of core-shell structured titanium alloy. *J. Alloy. Compd.* **2019**, *775*, 316–321. [[CrossRef](#)]
22. Feng, S.; Li, J.; Kou, H. Nano-precipitation and tensile properties of Ti60 alloy after exposure at 550 °C and 650 °C. *Mater. Sci. Eng. A* **2015**, *626*, 247–253.
23. Ramachandra, C.; Singh, V. Silicide Precipitation in Alloy Ti-6Al-5Zr-0.5Mo-0.25Si. *Metall. Mater. Trans. A* **1982**, *13*, 771–775. [[CrossRef](#)]
24. Flower, N. Phase equilibria and transformations in a Ti-Zr-Si system. *Metall. Mater. Trans. A* **1995**, *26*, 243–257.
25. Ramachandra, C.; Singh, V. Effect of silicide precipitation on tensile properties and fracture of alloy Ti-6Al-5Zr-0.5Mo-0.25Si. *Metall. Trans. A* **1985**, *16*, 227–231. [[CrossRef](#)]
26. Jia, W.; Zeng, W.; Yu, H. Effect of aging on the tensile properties and microstructures of a near-alpha titanium alloy. *Mater. Des.* **2014**, *58*, 108–115. [[CrossRef](#)]
27. Ferreira, F.M.; de Oliveira, V.V.M.; Voorwald, H.J.C. Investigation of the damage and fracture of Ti-6Al-4V titanium alloy under dwell-fatigue loadings. *Procedia Struct. Integr.* **2022**, *35*, 141–149.

28. Zhou, Y.G.; Zeng, W.D.; Yu, H.Q. An investigation of a new near-beta forging process for titanium alloys and its application in aviation components. *Mater. Sci. Eng. A* **2004**, *393*, 204–212. [[CrossRef](#)]
29. Su, Y.; Hao, G.; Fan, H. Study on rolling of a new near- $\alpha$  titanium alloy: Microstructure refinement and dual-scale silicides evolution. *J. Alloy. Compd.* **2020**, *852*, 156867. [[CrossRef](#)]
30. Chen, X.; Qiu, C. Development of a novel metastable beta titanium alloy with ultrahigh yield strength and good ductility based on laser power bed fusion. *Addit. Manuf.* **2021**, *49*, 102501. [[CrossRef](#)]
31. Shang, C.; Zhang, F.; Zhang, B. Interface microstructure and strengthening mechanisms of multilayer graphene reinforced titanium alloy matrix nanocomposites with network architectures. *Mater. Des.* **2020**, *196*, 109119. [[CrossRef](#)]
32. Mittemeijer, E.J. *Fundamentals of Materials Science*; Springer: Berlin/Heidelberg, Germany, 2010.
33. Joseph, S.; Lindley, T.C.; Dye, D. Dislocation interactions and crack nucleation in a fatigued near-alpha titanium alloy. *Int. J. Plast.* **2018**, *110*, 38–56. [[CrossRef](#)]
34. Valiev, R.; Chmelik, F.; Bordeaux, F.; Kapelski, G.; Baudelet, B. The Hall-Petch relation in submicro-grained Al-1.5% Mg alloy. *Scr. Metall. Mater.* **1992**, *27*, 855–860. [[CrossRef](#)]
35. Hertzberg, R.W. Deformation and fracture mechanics of engineering materials. *J. Eng. Mater. Technol.* **1976**, *99*, 96. [[CrossRef](#)]

**Disclaimer/Publisher's Note:** The statements, opinions and data contained in all publications are solely those of the individual author(s) and contributor(s) and not of MDPI and/or the editor(s). MDPI and/or the editor(s) disclaim responsibility for any injury to people or property resulting from any ideas, methods, instructions or products referred to in the content.